

Earthquake statistics and plastic events in soft-glassy materials

Roberto Benzi,¹ Pinaki Kumar,² Federico Toschi² and Jeannot Trampert³

¹*Department of Physics, University of “Tor Vergata”, Via della Ricerca Scientifica 1, I-00133 Rome, Italy*

²*Department of Physics, Eindhoven University of Technology, PO Box 513, 5600 MB, Eindhoven, The Netherlands*

³*Department of Earth Sciences, Utrecht University, PO Box 80115, NL-3508 TC, Utrecht, The Netherlands. E-mail: jeannot@geo.uu.nl*

Accepted 2016 September 26. Received 2016 September 21; in original form 2016 January 12

SUMMARY

We propose a new approach for generating synthetic earthquakes based on the physics of soft glasses. The continuum approach produces yield-stress materials based on Lattice–Boltzmann simulations. We show that if the material is stimulated below yield stress, plastic events occur, which have strong similarities to seismic events. Based on a suitable definition of displacement in the continuum, we show that the plastic events obey a Gutenberg–Richter law with exponents similar to those for real earthquakes. We also find that the average acceleration, energy release, stress drop and interoccurrence times scale with the same exponent. Furthermore, choosing a suitable definition for aftershocks, we show that they follow Omori’s law. Finally, the far field power spectra of elastic waves generated by these plastic events decay as ω^{-2} similar to those observed for seismic waves. Our approach is fully self-consistent and all quantities can be calculated at all scales without the need of ad hoc friction or statistical assumptions. We therefore suggest that our approach may lead to new insights into the physics connecting the micro- and macroscales of earthquakes.

Key words: Probability distributions; Earthquake dynamics; Statistical seismology.

1 INTRODUCTION

It is well established that materials failing under compression or shear show a power-law behaviour of intermittent slip (e.g. Ben-Zion *et al.* 2011; Uhl *et al.* 2015). This power-law behaviour is observed over many length scales for a wide range of materials, as well as for many other natural and social processes, but what is responsible for the scale invariance is still under debate (Newman 2006). What further complicates the search for the cause of the power-law behaviour is that many phenomena show an exponential cut-off, below which the power law breaks down. For forced materials, this cut-off seems to depend on the applied force (Uhl *et al.* 2015). Furthermore, different loading modes (stress or strain rate) result in a similar power law, if analysed with a mean-field model, and can only be separated by analysing the time series in more detail (Maaß *et al.* 2015).

Earthquakes are the result of a mechanical failure of earth materials, and the power-law behaviour of their occurrence frequency is well established and known under the name of Gutenberg–Richter (GR) law (Gutenberg & Richter 1954). The details, however, of the underlying physics of why earthquakes occur, especially at the microscopic scale, are currently not understood. At the macroscopic scale, many aspects of earthquakes show a complex behaviour that can be modelled with tools of statistical and continuum physics. Earthquakes obey several empirical power laws possessing a certain scale invariance. The best known laws are the above mentioned GR law, which relates the frequency of earthquakes to their

magnitude or seismic moment (energy) and Omori’s law (Omori 1894; Utsu *et al.* 1995), which describes how the frequency of aftershocks decays with time. Other laws are less well documented, and for comprehensive overviews consult Rundle *et al.* (2003) and Turcotte *et al.* (2007). The reason for the power-law behaviour of earthquakes is still under debate. This is similar to other phenomena exhibiting power laws, for which the mechanisms are equally poorly understood. Scale invariance has been central in statistical physics in the context of self-organized criticality, which is known to produce a power-law behaviour (e.g. Newman 2006). If the earth is in a permanent critical state due to inherent dynamics, self-organized criticality could explain the power-law behaviour of earthquakes. Certain aspects of earthquakes, however, are better represented by characteristic earthquakes giving rise to characteristic energy and time scales. There is also some evidence that ‘mode-switching’ between several dynamical regimes occurs. The latter behaviour can be understood in terms of generalized phase changes between discrete and continuum states of material. An overview of these discussions can be found in Turcotte *et al.* (2007), Ben-Zion (2008) and Ben-Zion *et al.* (2011).

Deciding between scale invariance, characteristic scales or ‘mode-switching’ is a difficult problem because the dynamics involved (stress, strain, rupture velocity, friction, ...) is not directly observable. The problem is mostly approached by generating synthetic earthquake catalogues and comparing those to the observed GR law and/or Omori’s law from recorded earthquake catalogues. These synthetic catalogues are generated by either statistical models, or

mechanical models, and even a mixture of both. An overview of the commonly employed models can be found in Turcotte *et al.* (2007) and Vere-Jones (2011). The ETAS (epidemic-type aftershock sequence) model, for instance, is a popular statistical model, whereas the block-slider model is a popular mechanical one where everything is determined by the prescribed friction law (e.g. Kawamura *et al.* 2012). The block-slider model is most often implemented numerically (for a review see Rundle *et al.* 2003), although laboratory based studies are sometimes conducted (e.g. Rubinstein *et al.* 2011). None of these synthetic earthquake models provide a fundamental insight into the physics of earthquakes at the microscopic scale, which is ultimately responsible for the empirical laws seen for real earthquakes. The sequences are generated by ad-hoc prescribed statistical or constitutive laws. A popular constitutive law is the rate and state friction law (Dieterich 1979; Ruina 1983). This law is entirely phenomenological and the tuning of the parameters is based on laboratory experiments, although extrapolations from laboratory experiments to the earth's crust remain debated (e.g. Kanamori & Heaton 2000). An interesting recent development is the shear transition zone friction law (e.g. Daub & Carlson 2010), which is derived from physical processes acting at the grain scale, and captures the full range of rupture modes observed at the fault scale.

Another way to obtain catalogues is by controlled experiments. Since the pioneering study of (Mogi 1962), acoustic emissions of fracture experiments in the laboratory were monitored and their power-law behaviour studied. An overview of earlier studies can be found in (Rundle *et al.* 2003). Laboratory based fracture experiments are performed under controlled dynamic fracture regimes and the rupture can be observed from inception to arrest. Yoshimitsu *et al.* (2014) showed that there is a natural continuation in the scaling between seismic moment and corner frequency from kilometre-size natural earthquakes and millimetre-scale microruptures in rocks. A notable experiment following seismic scaling laws, for instance, is that of breaking bamboo chopsticks (Tsai *et al.* 2016).

We propose a new approach for generating synthetic earthquake catalogues, which is based on the physics of complex soft-glassy materials. This continuum approach, based on the Lattice-Boltzmann method, provides a way to simulate yield-stress materials (i.e. viscous fluid-like behaviour above a critical yield stress and plastic solid-like below the critical yield stress) (Benzi *et al.* 2010). Below yield stress, plastic (or brittle) events can be identified radiating elastic perturbations through the model (Benzi *et al.* 2014) similar to earthquakes. In this paper, we show that these plastic events follow the GR law with b -values comparable to those for observed earthquakes, as well as Omori's law, and generate elastic waves with power spectra proportional to ω^{-2} above a cut-off frequency. This is quite remarkable since we have made no special effort to tune our system to represent a realistic fault with a certain slip-behaviour or earth-like rock or gouge properties. Our approach is not based on any phenomenological laws but on the exact momentum equations of a mixture of immiscible fluids. It is important to note that yield stress is not imposed by our approach, but a consequence of the prescribed repulsion and attraction potentials and the distribution functions of the fluids. We force the system below yield stress to make it behave like a solid, where elastic waves are generated by plastic events. This is quite different to the classical continuum approach used for modelling fault zones, which is based on the rate-and-state friction law. This phenomenological law characterizes the dependence of friction on slip, slip velocity, slip history and normal stress. The parameters are often calibrated by laboratory experiments and the modelling is very successful in

reproducing earthquake statistics (see e.g. Ben-Zion 2008; Daub & Carlson 2010).

In our approach, all physical properties can be computed at any scale (Benzi *et al.* 2014, 2015). We speculate that a properly tuned system and a more detailed comparison with real earthquake data could yield insight into the physics responsible for the observed power laws in Earth's seismicity. We finally remark that, recently a similar approach to ours has been proposed using molecular dynamics simulations for glass forming systems (see for instance Salerno & Robbins 2013; Lin *et al.* 2014; Liu *et al.* 2016).

2 GENERATING PLASTIC EVENTS AND THEIR ANALYSIS

We consider a system of soft glass recently introduced into the literature (Benzi *et al.* 2009) and based on a lattice kinetic description. The basic idea of the approach is to consider two non-ideal fluids with particular frustration effects at the interface in order to stabilize phase separation against coarsening. In particular, we use a mesoscopic lattice Boltzmann model for non-ideal binary fluids, which combines a small positive surface tension, promoting highly complex interfaces, with a positive disjoining pressure, inhibiting interface coalescence. The mesoscopic kinetic model considers two fluids A and B , each described by a *discrete* kinetic distribution function $f_{\zeta i}(\mathbf{r}, \mathbf{c}_i; t)$, measuring the probability of finding a particle of fluid $\zeta = A, B$ at position \mathbf{r} and time t , with a discrete velocity \mathbf{c}_i , where the index i runs over the nearest and next-to-nearest neighbours of \mathbf{r} in a regular 2-D lattice. \mathbf{c}_i represents a 'molecular' or mesoscopic velocity of order $1/\sqrt{3}$ in our simulations. The system is further characterized by elastic (shear and pressure) waves with speeds about 30 times slower than the mesoscopic velocity (Benzi *et al.* 2014). The mesoscale particle represents all molecules contained in a unit cell of the lattice. The distribution functions evolve with time under the effect of free-streaming and local two-body collisions, described, for both fluids ($\zeta = A, B$), by a relaxation towards a local equilibrium ($f_{\zeta i}^{(eq)}$) with a characteristic time-scale τ_{LB} :

$$\begin{aligned} f_{\zeta i}(\mathbf{r} + \mathbf{c}_i, \mathbf{c}_i; t + 1) - f_{\zeta i}(\mathbf{r}, \mathbf{c}_i; t) \\ = -\frac{1}{\tau_{LB}} \left(f_{\zeta i} - f_{\zeta i}^{(eq)} \right) (\mathbf{r}, \mathbf{c}_i; t) + F_{\zeta i}(\mathbf{r}, \mathbf{c}_i; t). \end{aligned} \quad (1)$$

The equilibrium distribution is given by

$$f_{\zeta i}^{(eq)} = w_i \rho_{\zeta} \left[1 + \frac{\mathbf{u} \cdot \mathbf{c}_i}{c_s^2} + \frac{\mathbf{u} \cdot \mathbf{u} : (\mathbf{c}_i \mathbf{c}_i - c_s^2)}{2c_s^4} \right] \quad (2)$$

with w_i a set of weights known *a priori* (Sbragaglia & Shan 2011). Coarse grained hydrodynamical densities for both species are defined as $\rho_{\zeta} = \sum_i f_{\zeta i}$ and the global momentum for the whole binary mixture as $\mathbf{j} = \rho \mathbf{u} = \sum_{\zeta} \sum_i f_{\zeta i} \mathbf{c}_i$, with $\rho = \sum_{\zeta} \rho_{\zeta}$. The term $F_{\zeta i}(\mathbf{r}, \mathbf{c}_i; t)$ is the i th projection of the total internal force which includes a variety of interparticle forces. A delicate issue concerns the choice of the forcing term and is done as follows: First, we consider a repulsive (r) force with strength parameter \mathcal{G}_{AB} between the two fluids

$$\mathbf{F}_{\zeta}^{(r)}(\mathbf{r}) = -\mathcal{G}_{AB} \rho_{\zeta}(\mathbf{r}) \sum_{i, \zeta' \neq \zeta} w_i \rho_{\zeta'}(\mathbf{r} + \mathbf{c}_i) \mathbf{c}_i \quad (3)$$

which is responsible for the phase separation. Both fluids are also subject to competing interactions, which provide a mechanism for a *frustration* (F) of the phase separation. In particular, we introduce two forces, namely a short-range (nearest neighbour, NN)

self-attraction, controlled by strength parameters $\mathcal{G}_{\zeta,1} < 0$ and ‘long-range’ (next to nearest neighbour, NNN) self-repulsion, governed by strength parameters $\mathcal{G}_{\zeta,2} > 0$

$$\mathbf{F}_{\zeta}^{(F)}(\mathbf{r}) = -\mathcal{G}_{\zeta,1}\psi_{\zeta}(\mathbf{r})\sum_{i\in\text{NN}}w_i\psi_{\zeta}(\mathbf{r}+\mathbf{c}_i)\mathbf{c}_i - \mathcal{G}_{\zeta,2}\psi_{\zeta}(\mathbf{r})\times\sum_{i\in\text{NNN}}w_i\psi_{\zeta}(\mathbf{r}+\mathbf{c}_i)\mathbf{c}_i \quad (4)$$

with $\psi_{\zeta}(\mathbf{r}) = \psi[\rho_{\zeta}(\mathbf{r})] = 1 - e^{-\rho_{\zeta}(\mathbf{r})}$ a suitable pseudo-potential function (Shan & Chen 1993). Despite their inherent microscopic simplicity, the above dynamic rules are able to promote a host of non-trivial collective effects (for a detailed discussion see Benzi *et al.* 2009). By properly tuning the phase separating interactions (3) and the competing interactions (4), the model simultaneously achieves a small positive surface tension Γ and a positive disjoining pressure Π_d . In short, particles sitting at the interface are subject to three different forces: an attractive one from the NN particles of the same species and *two* repulsive forces from the NNN particles of the same species and the NN particles of the other species. The two opposite repulsion forces introduce a frustration effect at the interface which is able to dramatically slow down the coarsening effect in the system. This allows the simulations of droplets of one dispersed phase into the other, which are stabilized against coalescence. Once the droplets are stabilized, different packing fractions and poly dispersity of the dispersed phase can be achieved. In the numerical simulations presented in this paper, the packing fraction of the dispersed phase in the continuum phase is kept approximately equal to 90 per cent. The model provides two basic advantages whose combination is not common: On the one hand, it provides a realistic structure for the emulsion droplets, like for instance the Surface Evolver method; at the same time, due to its built-in properties, the model gives directly access to equilibrium and out-of-equilibrium shear-stresses, including both elastic and viscous contributions.

Upon choosing a small volume ratio between the two fluids (say the volume of fluid A divided by that of fluid B is small), the model exhibits a typical configuration depicted in Fig. 2 that closely resembles that observed in real emulsions and foams. The model shows remarkable agreement with existing experimental data, namely we observe a finite yield stress σ_y above which the shear-stress σ depends on the strain-rate S following a Herschel–Bulkley law (Benzi *et al.* 2014; Dollet *et al.* 2015). In Fig. 1, we show the shear-stress σ as a function of external strain-rate S in a standard Couette geometry, where the external strain-rate is due to the imposed boundary conditions.

For a small external strain-rate S , the system does not flow. The external forcing provides the energy for isolated plastic rearrangements which usually take the form of a so called T1 events (e.g. Benzi *et al.* 2014). In Fig. 2, we give an example of such plastic events, which can be isolated in space-time or multiple events can occur simultaneously (avalanches). In all cases, just a few bubbles change the topological network of the system. Soon after a plastic event, elastic waves travel through the domain and can trigger other plastic events. The overall dynamics is strongly intermittent in space and time, a feature often observed in laboratory visualization of real emulsions. A standard Voronoi tessellation is able to capture the topological change in the network and the location of plastic events. Remarkably, our model is perhaps the only one which enables the simulation of an emulsion-like system with realistic interface dynamics and with no *a priori* constraints on bubble sizes and shapes.

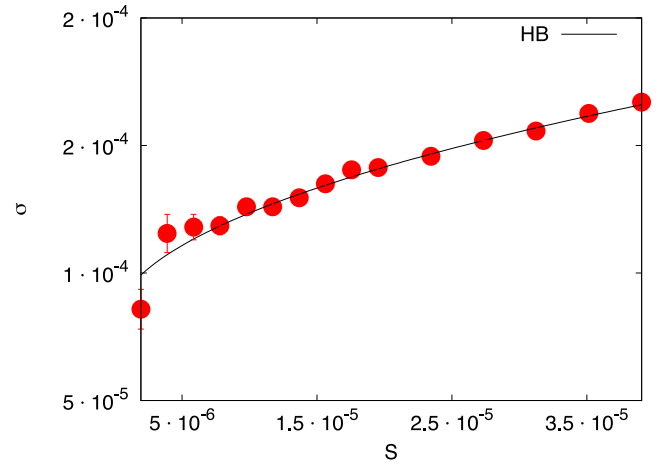


Figure 1. Shear-stress σ as a function of the imposed strain-rate S for a Couette geometry, obtained by using the Lattice–Boltzmann model described in the text. The best fitting Herschel–Bulkley law is also shown. The red dots represent values for stress in our simulations for different strain-rates, and show the existence of a yield stress in our simulated materials.

For a small external strain-rate S , the shear-stress $\sigma(t)$ in the system is smaller than the yield stress σ_y and the system exhibits stick-slip behaviour. Such an intermittent stop-and-go mechanism has often been thought of as the basic mechanism underlying the statistical properties of earthquake dynamics (e.g. Rundle *et al.* 2003; Ben-Zion 2008; Kawamura *et al.* 2012; Lieou *et al.* 2015). Evidence for the occurrence of plastic events in our system has been given in Benzi *et al.* (2014). In Fig. 3, we show the behaviour of $\sigma(t)$ and the corresponding value of dv/dt for a relatively short time window in a simulation using a Couette geometry. $\sigma(t)$ is the space averaged stress and $v(t)$ is the velocity of the system averaged in space in the x direction and computed at the centre of the channel. In this example, we took a symmetric forcing on the two boundaries where the velocity difference $\Delta U = SL$ is fixed, S being the apparent external strain-rate and L the size of the system. We considered a system of 512^2 grids points corresponding to about 130 bubbles, where $S = 2.7 \times 10^{-6}$ and integrated the system for 3×10^7 time steps. For more information on the system equations, see (Benzi *et al.* 2014). In this particular case, the yield stress is $\sigma_y \approx 10^{-4}$. There are two remarkable features in Fig. 3: first of all, the stress $\sigma(t)$ intermittently shows strong drops followed by slow increases; second the acceleration dv/dt sporadically shows large fluctuations around a mean value of zero, reminiscent of earthquake recordings. Both effects are related to the above mentioned stick-slip mechanism. In particular, the large fluctuations in dv/dt correspond to plastic events in the system, which can be far or close from the central line where we measured $v(t)$.

While Fig. 3 looks encouraging and we are tempted to associate events corresponding to strong fluctuations in dv/dt to ‘earthquakes’, the quantity dv/dt is an average quantity and not suitable for a systematic investigation of the statistical properties of earthquake-like events. In seismology the statistical properties of earthquakes are investigated by looking at the frequency of earthquakes above a given magnitude, which are known to follow the GR law. To define magnitude or seismic moment, we need to define a suitable measure of displacement or slip.

Let us recall that the simulation uses kinetic equations in the continuum limit. Thus we have no particle we can follow in the system. However, because the interface between the two fluids is stable, we can measure displacements by computing changes in the

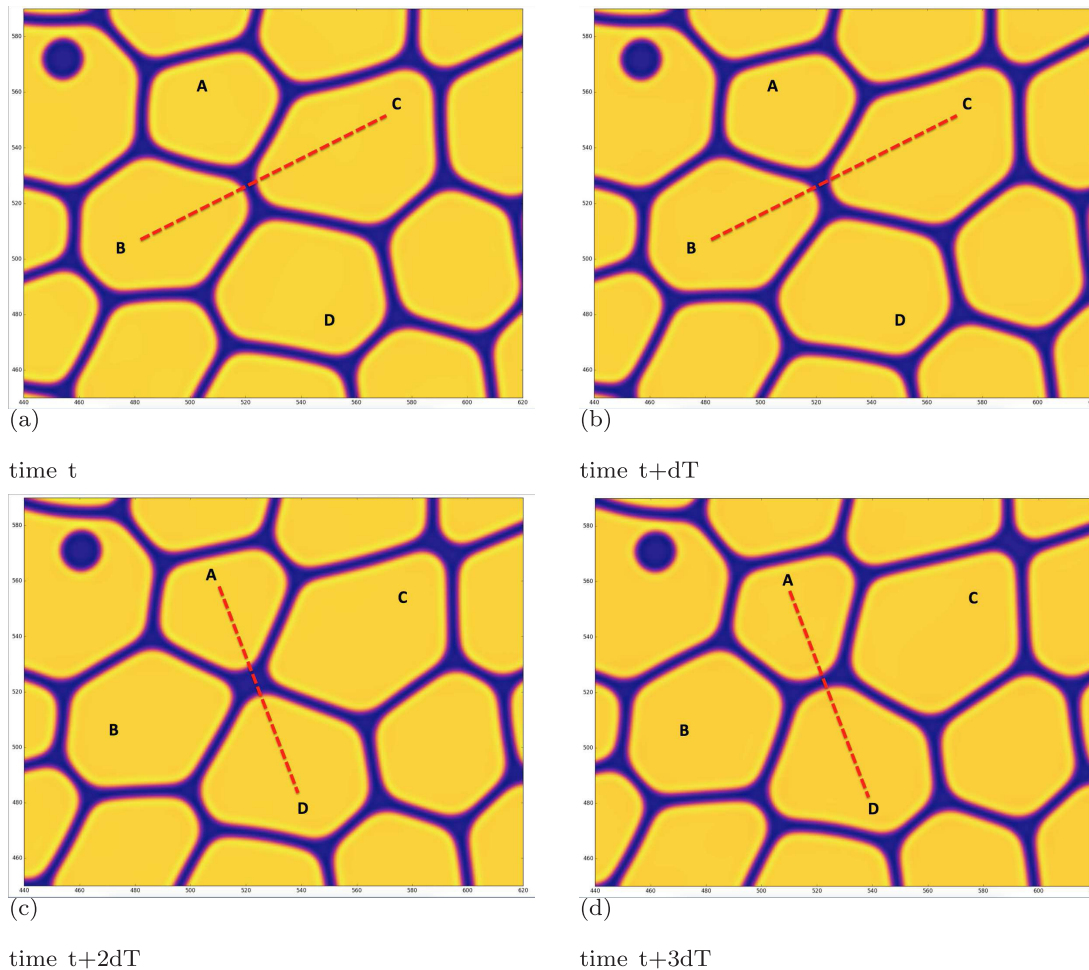


Figure 2. A typical plastic event observed in the numerical simulation of our Lattice–Boltzmann model. The figure shows a local enlargement of the density field at four different times. The red lines indicate two bubbles which are in contact. (a) At time t , bubbles B and C are closest. (b) At time $t + dT$, these bubbles have started moving apart. (c) At time $t + 2dT$, bubbles A and D are closest. (d) At time $t + 3dT$, A and D have moved even closer to each other. These movements represent a plastic event and correspond to an irreversible change in the topological configuration of the bubbles. The orange colour represents the high density fluid and the blue colour the lower density one. dT is smaller than τ chosen in Section 2.

position of the interface. The simplest way to do this is to take our system $L \times L$ and divided it into smaller squares of size $L/n \times L/n$. We chose n such that L/n corresponds to 32 grid points which is the average size of a single bubble. Furthermore we checked that our results, as discussed below, are independent of the exact choice of n . Next, for each square $L/n \times L/n$ we considered two consecutive times, say t and $t + \tau$ and computed the density change $\delta\rho(x, y, t, \tau) \equiv \rho(x, y, t + \tau) - \rho(x, y, t)$. Finally, we took the average of $\delta\rho(x, y, t, \tau)^2$ in square i , where i is a label for the n^2 squares of sides L/n and denoted it by $\delta\rho_i^2(t, \tau)$. The reason to choose $\delta\rho_i^2(t, \tau)$ is that for small enough τ , it is easy to show that $\delta\rho_i^2(t, \tau) \sim \rho^2 \mathcal{A}_i(t, \tau)$ where \mathcal{A}_i is the fraction of n^2 points which have been changed due to interface displacement. The value of $\mathcal{A}_i(t, \tau)$ is also proportional to $1 - O_i(t, \tau)$, where $O_i(t, \tau)$ is the so-called overlap between two consecutive configurations (e.g. Benzi *et al.* 2014).

We now need to connect our previously defined quantities to the standard definition of earthquake magnitude or moment. The seismic moment M_0 is defined as $M_0 \sim DS_a$, where D is the average slip of the earthquake and S_a its source area. For each small square, the area S_a is simply given by $(L/n)^2$ and the displacement is proportional to $\sqrt{\mathcal{A}_i(t, \tau)}$. However, $\mathcal{A}_i(t, \tau)$ shows strong fluctuations both in space (i.e. from square to square i) and in time (only at times where a plastic event occurs are one or more

values of \mathcal{A}_i relatively large). Therefore it seems reasonable to consider $D^2 \sim A(t, \tau) = \sup_i [\mathcal{A}_i(t, \tau)]$ as being representative of the squared-displacement. Such a choice is further motivated by the fact that plastic events are local in space and are responsible for the largest value of \mathcal{A}_i in i , and we are interested to study the statistical properties of the extreme events in the displacement, which corresponds to $A(t, \tau)$. Similarly in seismology, the maximum displacement at a given frequency is used to define a magnitude. In Fig. 4, we show the behaviour of $A(t, \tau)$ as a function of time for the same time snapshot as already discussed in Fig. 3. We observe a strong correlation in the sharp increase of $A(t, \tau)$ and a drop in stress $\sigma(t)$. It is interesting to note that some events occur in isolation whereas others cluster in time to form avalanches. In the following we take τ to be a relatively small fraction (0.2) of the characteristic time scale t_p for plastic events. In fact, plastic events occur over a small but non-zero value of time called t_p (Benzi *et al.* 2014). In our simulations $t_p \sim 5000$ time steps and we chose $\tau = 1000$ time steps. Hereafter, we will neglect τ in the definition of $A(t)$. The above discussion tells us that we can consider $M_0 \sim A(t)^{1/2}$. Within the same approximation, we can further estimate the energy release as $E_r \sim \Delta\sigma DS_a \sim D^2 \sqrt{S_a} \sim A(t)$, where $\Delta\sigma$ is the stress drop during an event, which is proportional to the local strain $D/\sqrt{S_a}$ (e.g. Madariaga 2011).

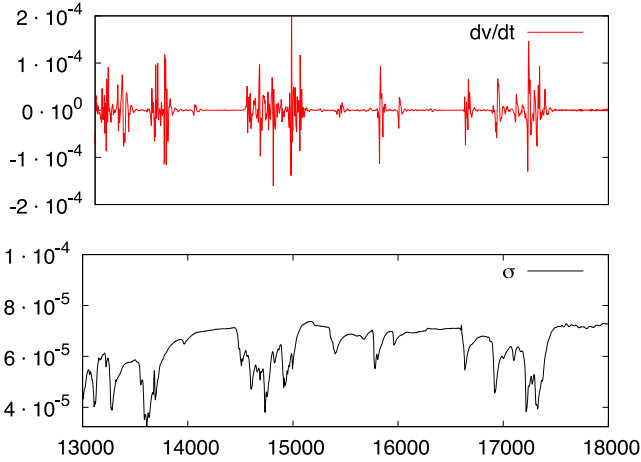


Figure 3. Behaviour of dv/dt , upper panel and shear-stress σ during a relatively short time period in the numerical simulation. The system is driven at the boundaries by a very small external strain-rate S in a Couette geometry. The velocity v has been obtained as the x average in the system at the centre of the channel. The shear stress σ is averaged over space in both x and y directions.

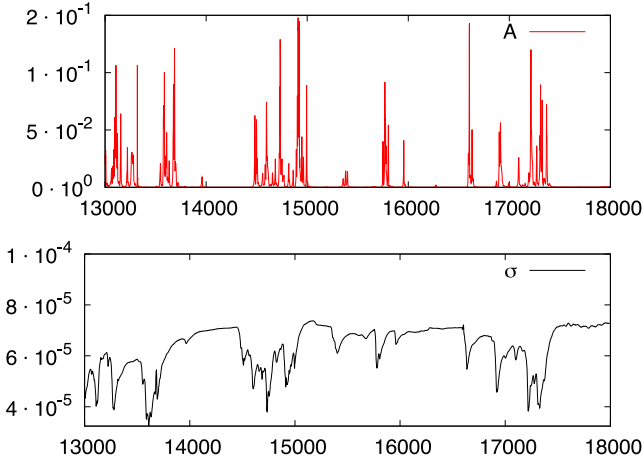


Figure 4. Same as in Fig. 3 with the upper panel representing the quantity $A(t)$ which provides a measure of the largest slip observed in the system.

3 RESULTS

Above we argued that $A(t)$ is a good candidate to investigate the statistical properties of our system. If that is the case, the GR law implies a scaling behaviour of the probability density distribution of A of the form:

$$P(A) \sim A^{-\gamma} \quad (5)$$

To assess the validity of eq. (5), we performed two different series of numerical simulations with resolution 512^2 and 1024^2 respectively. By increasing the resolution we increase the size of the system, that is, the number of bubbles. Numerical simulations were performed for several millions of time steps, long enough to assure the statistically invariance of the probability density function. For each resolution we chose two different values of the external forcing with $\sigma < \sigma_y$.

In Fig. 5, we show a ln-ln plot of $P(A)$ for two different values of the strain rate S for a resolution 512^2 . For both values of the strain rate a clear scaling of $P(A)$ is observed with exponents γ in the range [1.2, 1.4]. In order to assess the robustness of our results, we also computed the probability distribution of dv/dt and of the energy

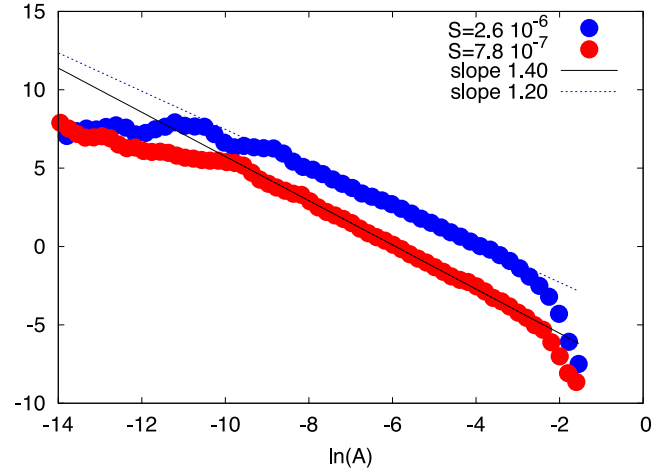


Figure 5. ln-ln plot of the probability distribution $P(A)$ of $A(t)$ obtained by numerical simulations for two different values of the strain-rate. $A^{1/2}$ is proportional to the seismic moment M_0 .

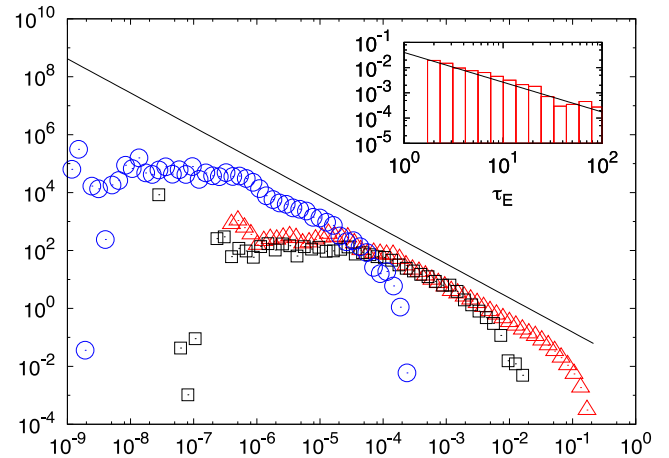


Figure 6. Probability density distribution for different quantities: red triangles correspond to the probability density of A and is the same as the one shown in Fig. 5 for the larger strain rate; blue circles correspond to the probability density function of $|dv/dt|$, where v is the average velocity in the x direction at the centre of the channel; the black squares corresponds to the probability distribution of the energy release E_r . In the insert we show the probability density function of τ_E defined as the time between two consecutive events. We define an event by the condition $A_{th} > 10^{-3}$. The black line in the insert has the same slope as the black line in the main part of the figure.

release in the system, namely $E_r \sim \sigma d\sigma/dt$. We assume that the elastic energy in the system is proportional to σ^2 and we compute the probability distribution of E_r for $E_r < 0$. In Fig. 6, we show the results for the probability distribution of A for the largest strain rate of Fig. 5 together with the probability distribution of $|dv/dt|$ and E_r . All quantities show almost the same scaling properties, although the range where the scaling law is observed is somewhat quantity dependent. The figure clearly shows that $E_r \sim A(t)$ as we stated at the end of Section 2, although E_r was obtained by an independent calculation in this figure. Remarkably, the same scaling law seems to be observed for the time τ_E between two consecutive events. In particular, we defined an event when $A(t)$ is greater than a given threshold A_{th} which, for Fig. 6, is chosen to be $A_{th} = 10^{-3}$. In the insert of Fig. 6, we show the probability distribution of τ_E where the black line corresponds to the scaling law observed in Fig. 5. If aftershocks dominate the distribution of these interoccurrence

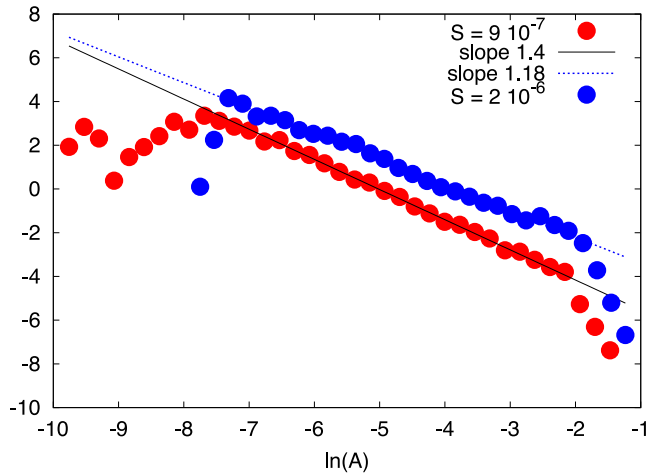


Figure 7. Same as in Fig. 5 for a simulation at a resolution of 1024^2 . Note that by increasing the resolution we are increasing the system size, that is, the number of bubbles.

times, we would expect to recover Omori's law (see discussion in Turcotte *et al.* 2007). Finally in Fig. 7, we show the probability distribution of $A(t)$ for the numerical results using a resolution of 1024^2 .

To investigate Omori's law, we adopted the distance metric introduced by Baiesi & Paczuski (2004). Using our variables, we rewrote it as $n_{pq} = \Delta T (\Delta L)^{d_f} 10^{-B_{GR} \log A_p}$ for every pair of events (p, q) and where $p < q$, that is, event p occurred before q . ΔT is the time difference (in LB units) between events, ΔL their distance separation and d_f is the fractal dimension of the interface, which is 1.5 in our case. B_{GR} is the slope in the Gutenberg–Richter law for the moment and derived from Fig. 5 (see below), and A_p is the squared displacement for event p . The use of this NN metric for the statistical classification of earthquakes into aftershocks and background seismicity was introduced by Zaliapin *et al.* (2008) and Zaliapin & Ben-Zion (2013). The inverse of n_{pq} can be interpreted as a proxy for the degree to which events are correlated. By determining a threshold for this correlation, we can identify aftershock sequences. We set this threshold to be close to the inverse value of the antimode in the bi-modal probability distribution function of the nearest-neighbour distance corresponding to our case, as outlined by Zaliapin & Ben-Zion (2013). We then chose the 1000 strongest events and their corresponding aftershocks and plot the probability density rate of plastic events as a function of time from the main event. We find that the rate of events aligns along a line as predicted by Omori's law (Fig. 8). We verified that the result is robust with respect to the choice of this threshold, and changing it even by an order of magnitude does not significantly affect the result.

We also looked at the power spectra of \mathcal{A}_i at surface element i where no extreme values occur, that is, where $\mathcal{A}_i < A$ and no events occur for any time t . This is equivalent to looking at a power spectrum of the ground displacement generated by an earthquake in the far field. It is well established that the power spectra of seismic ground displacements are flat with a decay $\sim \omega^{-2}$ beyond a corner frequency (e.g. Aki & Richards 1980). In Fig. 9, we show the power spectra obtained in our numerical simulations, using a resolution of 1024^2 , exhibiting a characteristic ω^{-2} decay. This is further evidence that our system is capable of capturing features of real earthquakes.

The results shown in Figs 5–8 are independent of our choice of the effective displacement $D = A^{1/2}$. We have checked that the same scaling is observed, for instance, if we consider the quantity

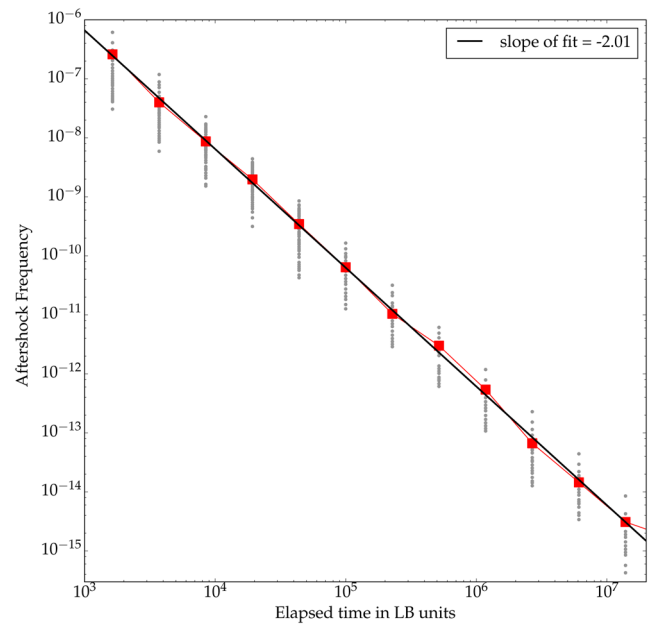


Figure 8. Rate of change in the number of aftershocks for fixed time bins corresponding to the 1000 strongest main events in our catalogue. The time is counted from the beginning of the corresponding main shocks. Red squares represent the mean for a particular bin.

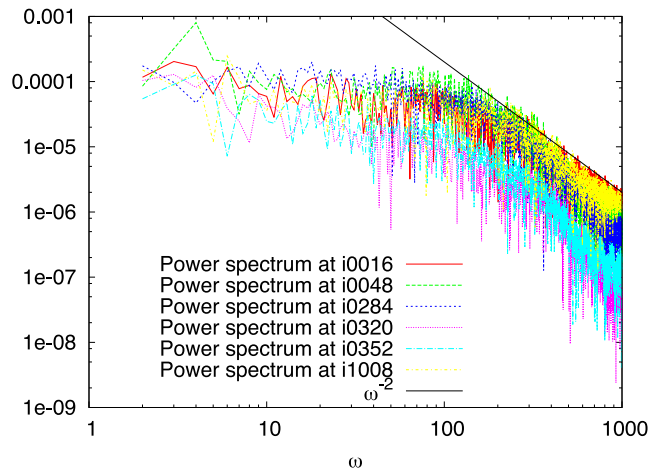


Figure 9. Power spectra of far field elastic displacements at several randomly chosen squares (i....) in the box. They show a clear ω^{-2} -decay.

$\tilde{A} \equiv N_{\text{eff}}^{-1} \sum_i \mathcal{A}_i(t)$ where N_{eff} is the number of small boxes where the displacement is concentrated. More specifically, upon defining $p_i \equiv \mathcal{A}_i(t) / \sum_i \mathcal{A}_i(t)$, we compute the 'entropy' $H \equiv -\sum_i p_i \log p_i$ and derived $N_{\text{eff}} \equiv \exp(H)$, which by definition is the number of boxes where the displacement is concentrated. It turns out that $\tilde{A} \sim A$ for all times and with very high accuracy. This supports our choice to consider $A(t)$ as an unbiased estimate of the area subject to an effective slip.

4 CONCLUDING REMARKS

The information obtained from Figs 5–8 is quite clear and striking: the system shows well defined scaling laws for various quantities and independent of the volume considered (i.e. independent on the number of bubbles). Fig. 9 further shows that the power spectra of

far field displacements follow an ω -square model. In particular, our results strongly support the following conclusions:

- (i) A clear power-law scaling of $P(A)$ as a function of A is observed;
- (ii) The scaling exponent lies in the range [1.2, 1.4] and is smaller for larger values of the external strain rate S ;
- (iii) The scaling behaviour does not depend on the numerical resolution and it is the same for the acceleration $|dv/dt|$, the energy release E_r and hence the stress drop, and the interoccurrence time τ_E ;
- (iv) For all analysed aftershock sequences, there is clear evidence that our system obeys Omori's law;
- (v) The power spectra of far field elastic waves generated by the plastic events decays as ω^{-2} .

To compare the values of our scaling exponents with the ones observed in the GR law for earthquakes, we have to remember that the moment $M_0 \sim DS$. In our case $D \sim A^{1/2}$ since A is a measure of an area, namely the number of unit squares subject to displacement. If $P(A) \sim A^{-\gamma}$ then the quantity $M_0 \sim D \sim A^{1/2}$ shows a probability density distribution $P(M_0) \sim M_0^{1-2\gamma}$. In seismology the scaling is normally reported for cumulative distributions and the scaling constant B_{GR} is defined as $C(M_0) = \int_{M_0}^{\infty} P(x) dx \sim M_0^{-B_{GR}} \sim M_0^{2-2\gamma}$. The results shown above therefore give an estimate of B_{GR} in the range [0.4, 0.8] nicely bracketing the scalings reported for real earthquakes, which on average is 2/3 (e.g. Ben-Zion 2008). The slope we observe for Omori's law is close to -2 , but we did not plot the rate of the cumulative number of aftershocks as is usually done in seismology (e.g. Ben-Zion 2008). If we take that into account, we get a slope of -1 , close to that for real earthquakes, and the cumulative number of earthquakes will logarithmically depend on time counted from the main shock.

It is interesting to observe that the scaling exponent decreases for increasing shear rate S . Eventually, for very large S , we expect the stress to overcome the yield stress and, at that point, the system starts to flow. Only in the region $\sigma < \sigma_y$ does the system show stick-slip behaviour and GR statistics. It is worth stressing that the statistical properties of $P(A)$ are resolution independent. Finally, we would like to reiterate that our model so far is not designed to represent any realistic seismic environment and/or a particular form of friction law, yet shows many characteristics of natural earthquakes.

ACKNOWLEDGEMENTS

This research was partly funded by the Shell-NWO/FOM programme 'Computational sciences for energy research' under project number 14CSER022.

REFERENCES

Aki, K. & Richards, P., 1980. *Quantitative Seismology: Theory and Methods*, Freeman.

Baiesi, M. & Paczuski, M., 2004. Scale-free networks of earthquakes and aftershocks, *Phys. Rev. E*, **69**, 066106, doi:10.1103/PhysRevE.69.066106.

Benzi, R., Sbragaglia, M., Succi, S., Bernaschi, M. & Chibbaro, S., 2009. Mesoscopic lattice Boltzmann modeling of soft-glass systems: theory and simulations, *J. Chem. Phys.*, **131**, 104903, doi:10.1063/1.3216105.

Benzi, R., Bernaschi, M., Sbragaglia, M. & Succi, S., 2010. Herschel–Bulkley rheology from lattice kinetic theory of soft glassy materials, *Europhys. Lett.*, **91**(1), 14003, doi:10.1209/0295-5075/91/14003.

Benzi, R., Sbragaglia, M., Perlekar, P., Bernaschi, M., Succi, S. & Toschi, F., 2014. Direct evidence of plastic events and dynamic heterogeneities in soft-glasses, *Soft Matter*, **10**, 4615–4624.

Benzi, R., Sbragaglia, M., Scagliarini, A., Perlekar, P., Bernaschi, M., Succi, S. & Toschi, F., 2015. Internal dynamics and activated processes in soft-glass materials, *Soft Matter*, **11**, 1271–1280.

Ben-Zion, Y., 2008. Collective behaviour of earthquakes and faults: Continuum-discrete transitions, progressive evolutionary changes and different dynamic regimes, *Rev. Geophys.*, **46**, RG4006, doi:10.1029/2008RG000260.

Ben-Zion, Y., Dahmen, K.A. & Uhl, J.T., 2011. A unifying phase diagram for the dynamics of sheared solids and granular materials, *Pure appl. Geophys.*, **168**, 2221–2237.

Daub, E.G. & Carlson, J.M., 2010. Friction, fracture, and earthquakes, *Annu. Rev. Condens. Matter Phys.*, **1**, 397–418.

Dieterich, J.H., 1979. Modeling of rock friction: 1. Experimental results and constitutive laws, *J. geophys. Res.*, **84**, 2161–2168.

Dollet, B., Scagliarini, A. & Sbragaglia, M., 2015. Two-dimensional plastic flow of foams and emulsions in a channel: experiments and lattice Boltzmann simulations, *J. Fluid Mech.*, **766**, 556–589.

Gutenberg, B. & Richter, C., 1954. *Seismicity of the Earth and Associated Phenomena*, Princeton Univ. Press.

Kanamori, H. & Heaton, T.H., 2000. Microscopic and macroscopic physics of earthquakes, in *GeoComplexity and the Physics of Earthquakes*, pp. 147–163, eds Rundle, J.B. et al., Geophysical Monographs, AGU.

Kawamura, H., Hatano, T., Kato, N., Biswas, S. & Chakrabarti, B., 2012. Statistical physics of fracture, friction and earthquakes, *Rev. Mod. Phys.*, **84**, 839–884.

Lieou, C.K.C., Elbanna, A., E. Langer, J.S. & Carlson, J.M., 2015. Stick-slip instabilities in sheared granular flow: the role of friction and acoustic vibrations, *Phys. Rev. E*, **92**, 022209, doi:10.1103/PhysRevE.92.022209.

Lin, J., Lerner, E., Rosso, A. & Wyart, M., 2014. Scaling description of the yielding transition in soft amorphous solids at zero temperature, *Proc. Natl. Acad. Sci. USA*, **111**(40), 14 382–14 387.

Liu, C., Ferrero, E.E., Puosi, F., Barrat, J.-L. & Martens, K., 2016. Driving rate dependence of avalanche statistics and shapes at the yielding transition, *Phys. Rev. Lett.*, **116**, doi:10.1103/PhysRevLett.116.065501.

Maaß, R., Wraith, M., Uhl, J.T., Greer, J.R. & Dahmen, K.A., 2015. Slip statistics of dislocation avalanches under different loading modes, *Phys. Rev. E*, **91**, 042403, doi:10.1103/PhysRevE.91.042403.

Madariaga, R., 2011. Earthquake scaling laws, in *Extreme Environmental Events*, pp. 364–382, ed. Meyers, R., Springer.

Mogi, K., 1962. Study of elastic shocks caused by the fracture of heterogeneous materials and its relations to earthquake phenomena, *Bull. Earthq. Res. Inst. Univ. Tokyo*, **40**, 125–173.

Newman, M.E.J., 2006. Power laws, Pareto distributions and Zipf's law, *Contemp. Phys.*, **46**, 323–351.

Omori, F., 1894. On the aftershock of earthquakes, *J. Coll. Sci. Imp. Univ. Tokyo*, **7**, 111–200.

Rubinstein, S., Barel, I., Reches, Z., Braun, O., Urbakh, M. & Fineberg, J., 2011. Slip sequences in laboratory experiments resulting from inhomogeneous shear as analogs of earthquakes associated with a fault edge, *Pure appl. Geophys.*, **168**(12), 2151–2166.

Ruina, A.L., 1983. Slip instabilities and state variable friction laws, *J. geophys. Res.*, **88**, 10 359–10 370.

Rundle, J., Turcotte, D., Shcherbakov, R., Klein, W. & Sammis, C., 2003. Statistical physics approach to understanding the multiscale dynamics of earthquake fault systems, *Rev. Geophys.*, **41**, 4/1019, doi:10.1029/2003RG000135.

Salerno, K.M. & Robbins, M.O., 2013. Effect of inertia on sheared disordered solids: critical scaling of avalanches in two and three dimensions, *Phys. Rev. E*, **88**(6), 062206, doi:10.1103/PhysRevE.88.062206.

Sbragaglia, M. & Shan, X., 2011. Consistent pseudopotential interactions in lattice Boltzmann models, *Phys. Rev. E*, **84**, 036703, doi:10.1103/PhysRevE.84.036703.

Shan, X. & Chen, H., 1993. Lattice Boltzmann model for simulating flows with multiple phases and components, *Phys. Rev. E*, **47**, 1815–1819.

- Tsai, S.-T., Wang, L.-M., Huang, P., Yang, Z., Chang, C.-D. & Hong, T.-M., 2016. Acoustic emission from breaking a bamboo chopstick, *Phys. Rev. Lett.*, **116**, 0035501, doi:10.1103/PhysRevLett.116.035501.
- Turcotte, D., Shcherbakov, R. & Rundle, J., 2007. Complexity and earthquakes, in *Treatise on Geophysics*, vol. Vol. 4, pp. 675–700, ed. Kanamori, H., Elsevier.
- Uhl, J.T. *et al.*, 2015. Universal quake statistics: from compressed nanocrystals to earthquakes, *Sci. Rep.*, **5**, 16493, doi:10.1038/srep16493.
- Utsu, T., Ogata, Y. & Matsu'ure, R., 1995. The centenary of the Omori formula for a decay law of aftershock activity, *J. Phys. Earth*, **43**, 1–33.
- Vere-Jones, D., 2011. Stochastic models for earthquake occurrence and mechanisms, in *Extreme Environmental Events*, pp. 338–363, ed. Meyers, R., Springer, New York.
- Yoshimitsu, N., Kawakata, H. & Takahashi, N., 2014. Magnitude -7 level earthquakes: a new lower limit of self-similarity in seismic scaling relationships, *Geophys. Res. Lett.*, **41**, 4495–4502.
- Zaliapin, I. & Ben-Zion, Y., 2013. Earthquake clusters in southern California I: identification and stability, *J. geophys. Res.*, **118**(6), 2847–2864.
- Zaliapin, I., Gabrielov, A., Keilis-Borok, V. & Wong, H., 2008. Clustering analysis of seismicity and aftershock identification, *Phys. Rev. Lett.*, **101**(1), 018501, doi:10.1103/PhysRevLett.101.018501.